# Phonon-Assisted Intervalley Scattering Determines Ultrafast Exciton Dynamics in $MoSe_2$ Bilayers

Sophia Helmrich,[1] Kevin Sampson,[2,3] Di Huang,[2] Malte Selig,[4] Kai Hao,[2] Kha Tran,[2] Alexander Achstein,[1] Carter Young,[2] Andreas Knorr,[4] Ermin Malic,[5] Ulrike Woggon,[1] Nina Owschimikow,[1,*] and Xiaoqin Li[2,3,†]

[1]*Department of Optics and Atomic Physics, Technical University Berlin, Berlin 10623, Germany*
[2]*Department of Physics and Center for Complex Quantum Systems, The University of Texas at Austin, Austin, Texas 78712, USA*
[3]*Center for Dynamics and Control of Materials and Texas Materials Institute, 2501 Speedway, Austin, Texas 78712, USA*
[4]*Nichtlineare Optik und Quantenelektronik, Institut für Theoretische Physik, Technische Universität Berlin, 10623 Berlin, Germany*
[5]*Department of Physics, Philipps University Marburg, 35037 Marburg, Germany*

(Received 19 September 2020; revised 23 April 2021; accepted 23 August 2021; published 8 October 2021)

While valleys (energy extrema) are present in all band structures of solids, their preeminent role in determining exciton resonances and dynamics in atomically thin transition metal dichalcogenides (TMDC) is unique. Using two-dimensional coherent electronic spectroscopy, we find that exciton decoherence occurs on a much faster timescale in $MoSe_2$ bilayers than that in the monolayers. We further identify two population relaxation channels in the bilayer, a coherent and an incoherent one. Our microscopic model reveals that phonon-emission processes facilitate scattering events from the $K$ valley to other lower-energy $\Gamma$ and $\Lambda$ valleys in the bilayer. Our combined experimental and theoretical studies unequivocally establish different microscopic mechanisms that determine exciton quantum dynamics in TMDC monolayers and bilayers. Understanding exciton quantum dynamics provides critical guidance to the manipulation of spin-valley degrees of freedom in TMDC bilayers.

DOI: 10.1103/PhysRevLett.127.157403

Much effort has been devoted to understanding the optical properties of semiconducting transition metal dichalcogenides (TMDCs) because of their unique layer-dependent band structures, strong light-matter interaction, and easy integration with other photonic structures [1,2]. In both TMDC monolayers (MLs) and bilayers (BLs), exciton resonances dominate optical absorption spectra, exhibiting large oscillator strength and binding energy. These bright excitons correspond to direct transitions at the $K$ points and follow unique optical selection rules, often referred to as spin-valley locking [3–6]. The significantly stronger photoluminescence (PL) intensity in MLs compared with BLs indicates a transition from a direct to indirect band gap [7,8]. Considering their similar absorption and markedly different PL, a question naturally arises: Is there any difference between the exciton quantum dynamics in TMDC MLs and BLs?

Our study focuses on $MoSe_2$ MLs and BLs. The transition from a direct gap in ML $MoSe_2$ to an indirect gap in the BL coincides with the emergence of multiple low-energy valleys as illustrated in Fig. 1(a). Valley scattering processes may strongly influence exciton quantum dynamics [9–12], which are characterized by two critical parameters: the population relaxation ($\Gamma = 1/T_1$) and decoherence rates ($\gamma = 1/T_2$). These quantum dissipative processes are related by $\gamma = 1/T_2 = 1/2T_1 + \gamma_{\mathrm{ph}}$, where $\gamma_{\mathrm{ph}}$ represents the pure dephasing. Exciton quantum dynamics in TMDC monolayers have

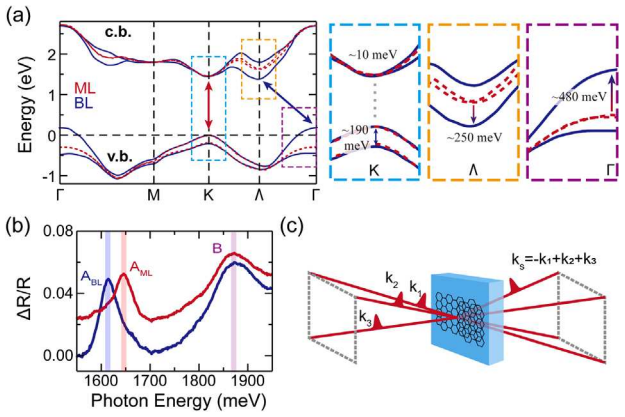


FIG. 1. (a) Single-particle band structures of $MoSe_2$ ML (red dashed lines) and BL (blue solid lines) with spin-orbit coupling, showing the two highest valence and the lowest conduction bands adapted from Roldan *et al.* [21]. Details of the band evolution from ML to BL at the $K$, $\Lambda$, and $\Gamma$ points are shown in the blue, orange, and purple rectangles at right. (b) Reflectance spectra for $MoSe_2$ ML (red) and BL (blue) at 30 K. (c) Schematic of the 2DCES experiment in a box geometry.

 

been investigated previously [13–19], and $K-K$ exciton coherence was found to be recombination limited. In contrast, many questions related to exciton dynamics remain unknown in bilayers because of their more complex valley structure, layer pseudospins, and indirect gaps [20].

Here, we apply two-dimensional coherent electronic spectroscopy (2DCES) to investigate intrinsic exciton quantum dynamics in a $MoSe_2$ BL in comparison to a ML. Our measurements reveal the ultrafast exciton decoherence time in $MoSe_2$ BLs to be ~50 fs at low temperature, corresponding to a homogeneous linewidth of $2\gamma \sim 27$ meV. This dephasing time is a factor of 6 shorter than that in the ML. We further distinguish two distinct population relaxation channels, a coherent population relaxation occurring on a timescale of ~55 fs, and an incoherent population relaxation that occurs at ~800 fs. Microscopic calculations yield excellent agreement with experiments and suggest that the ultrafast exciton dephasing and population relaxation in the BL originate from phonon-assisted intervalley scattering processes from the $K$ valley to other, lower-energy valleys (i.e., $\Lambda$ and $\Gamma$ valleys). An enhanced exciton decoherence arising from intervalley scattering is likely also present in other stacked and twisted TMDC BLs with momentum-indirect states below the optically bright excitons [22,23].

The $MoSe_2$ ML and BL are mechanically exfoliated from a bulk crystal and transferred to a sapphire substrate for optical measurements (more details in the Supplemental Material [24]). All optical measurements are performed at ~30 K unless otherwise specified. We observe two resonances in both the ML and BL in linear reflectivity measurements and attribute them to the $A$ and $B$ excitons. The $A$ exciton is red-shifted in the BL, but the $B$ resonance energy is nearly constant. This observation is consistent with earlier experiments and confirms the spectral uniformity of sample [37,38]. We extract a full width half maximum of ~45 meV and ~80 meV for the ML and BL, respectively, by fitting with a Voigt function. The dominant contribution to the exciton linewidth at low temperature in linear spectroscopy is inhomogeneous broadening.

The lowest two conduction and valence bands calculated from density functional theory (DFT) are displayed in Fig. 1(a). The $A$ exciton corresponds to the $K-K$ transition between the first valence band and the lowest conduction band while the energy splitting between the $A$ and $B$ excitons mostly results from the strong spin-orbit interaction in TMDCs [21]. Critically, these and other [39] DFT calculations show the emergence of lower-energy valleys in BLs, which leads to increased intervalley scattering and dramatically alters exciton quantum dynamics, as we show below. Although the energy of other valleys relative to the $K$ points is important to our theoretical model, the absolute transition energy in DFT calculations cannot be directly compared to experimentally observed exciton resonances because DFT routinely underestimates band gaps [40] and exciton binding energies are not included.

The 2DCES experimental setup has been described in detail in previous studies [13,14,16,41]. Briefly, three phase-stabilized, cocircularly polarized excitation laser pulses are derived from the same Ti:Sapphire laser with ~60 fs pulse duration and 76 MHz repetition rate, with adjustable time delays ($t_1$ and $t_2$) between them. We choose the cocircular polarization for all pulses to resonantly excite excitons in one $K$ valley. The three beams are arranged in the standard box geometry shown in Fig. 1(c) and focused to a single spot ~8 $\mu$m in diameter. The photon-echo or four-wave mixing signal is generated along the fourth corner of the box, characterized by wave vector $k_S = -k_1 + k_2 + k_3$. Both the amplitude and phase of the nonlinear signal are measured via spectral interference with a fourth reference pulse separated by a time delay $t_3$ from the third pulse.

We first investigate exciton decoherence by taking the one-quantum rephasing spectrum. As shown in Fig. 2(a), the one-quantum rephasing spectrum is obtained by scanning $t_1$ and $t_3$ while keeping $t_2$ constant. The time-domain signal is converted to the frequency domain via Fourier

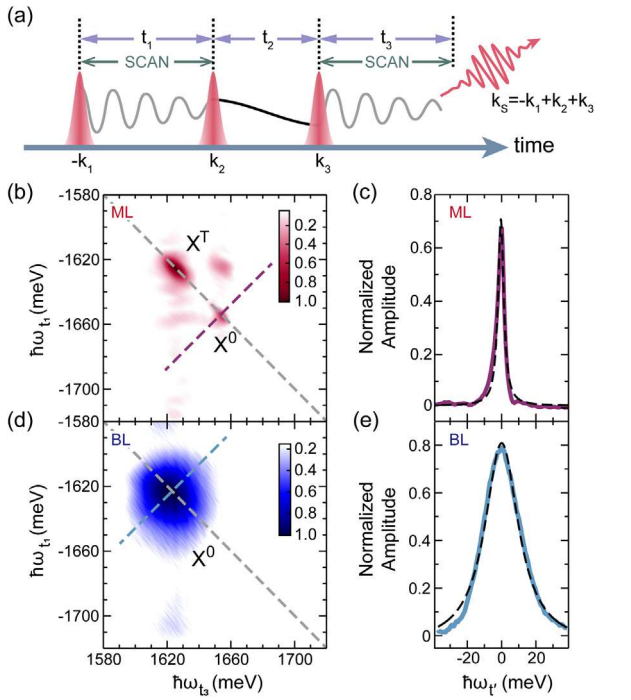


FIG. 2. One-quantum rephasing spectra from $MoSe_2$ ML and BL. (a) Schematic showing the one-quantum rephasing pulse sequence. (b),(d) Amplitude spectra of a $MoSe_2$ ML (BL) at $1 \times 10^{12}$ cm$^{-2}$ excitation density and 30 K. The exciton and trion resonances are indicated by $X^0$ and $X^T$ in the ML. The cross-diagonal linewidth (homogenous linewidth) is extracted at the $X^0$ peak indicated by the dotted line. (c),(e) The extracted homogeneous linewidths are fitted with Lorentzian functions for ML and BL $MoSe_2$, respectively. Here, $\omega_{t'} = \omega_{t_1} + \omega_{t_3}$.

transform. For the measurement presented here, $t_2 = 0$ fs is chosen. Elongation along the diagonal of the 2D spectrum is due to inhomogeneous broadening from variations in strain and dielectric environment, impurities, or defects [42]. In contrast, the cross-diagonal broadening along $\hbar\omega_{t_1} = -\hbar\omega_{t_3}$ reveals the intrinsic homogeneous linewidth $\gamma$, which is inversely proportional to the dephasing time $1/T_2 = \gamma$ [43].

The monolayer spectrum Fig. 2(b) features two prominent diagonal peaks attributed to the neutral exciton $X^0$ (1652 meV) and trion $X^T$ (1625 meV) [15,44], and coherent coupling between excitons and trions can be identified through the cross peaks. The $A$ exciton homogeneous broadening $\gamma^X_{\mathrm{ML}} = 2.1 \pm 0.2$ meV ($T^X_{2,\mathrm{ML}} = 313 \pm 33$ fs) is extracted from a Lorentzian fit for the exciton peak, shown in Fig. 2(c). All these features are consistent with previous studies [15,16,45].

In the 2D spectrum taken from the BL in Fig. 2(d), only one diagonal peak corresponding to the $A$ exciton at 1625 meV is observed over the spectral range covered by the excitation laser pulse ($1635 \pm 20$ meV). In contrast to the ML, the line shape of the exciton resonance in the $MoSe_2$ BL is nearly homogeneously broadened. Following a similar analysis, we extract a homogeneous broadening in Fig. 2(e) of $\gamma^X_{\mathrm{BL}} = 13.6 \pm 0.8$ meV ($T^X_{2,\mathrm{BL}} = 49 \pm 2$ fs). The excitons in bilayer $MoSe_2$ exhibit ~6 times faster dephasing than the ML $A$ excitons. While different substrates (e.g., $h$-BN) can alter exciton dephasing in ML by suppressing charge fluctuations or modifying the photon density [46], we anticipate a reduced substrate influence on BLs because of the rapid intervalley scattering.

To reveal the origin of exciton decoherence, we apply a microscopic theory that quantitatively evaluates the role of exciton-phonon interaction and intervalley scattering [10,47]. We start with the different ML and BL electronic band structures [Fig. 1(a)] from first-principle calculations, supported by ARPES experiments [48,49]. We then include excitonic effects by solving the Wannier equation, taking the modified Coulomb potential in ML and BL $MoSe_2$ into account [47,50]. The lowest lying exciton state $\nu = 1s$ is described by

$$E^{\xi_h\xi_e}_{\mathbf{Q}} = E^{\xi_h\xi_e}_0 + E^{\xi_h\xi_e 1s}_B + \frac{\hbar^2\mathbf{Q}^2}{2M^{\xi_h\xi_e}}, \qquad (1)$$

where the first term accounts for the energetic separation of the different intra- and intervalley transitions in the electronic picture, the second term accounts for the binding energy of the respective transition, and the third term accounts for the kinetic energy of the exciton with an effective mass $M^{\xi_h\xi_e} = m^{\xi_h}_h + m^{\xi_e}_e$.

The low-energy excitons consist of electrons and holes located at several high-symmetry points $\xi_{e/h}$ in the Brillouin zone, namely, $K(K')$, $\Lambda(\Lambda')$ points for electrons and $K(K')$, and $\Gamma$ points for holes. The threefold rotational

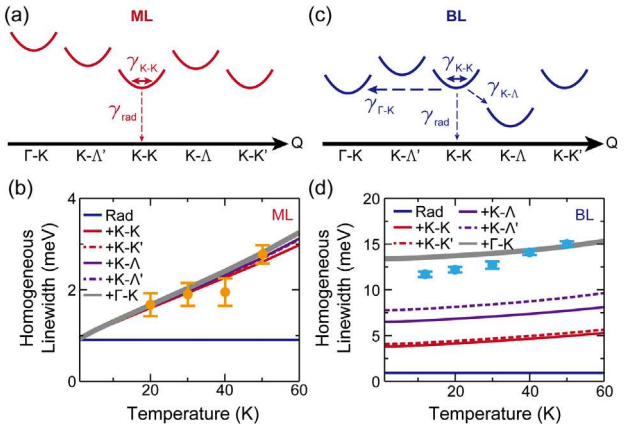


FIG. 3. Exciton dephasing as a function of temperature. (a),(c) Illustration of valley scattering processes influencing exciton dephasing in $MoSe_2$ (a) MLs and (c) BLs. The horizontal axis $Q$ stands for center-of-mass momentum, and vertical axis represents exciton energy. (b),(d) Calculated dephasing channels for ML (b) and BL (d), respectively. Linewidth broadening due to contributions from radiative decoherence, exciton intravalley scattering ($K - K$), and intervalley scattering to $K - K'$, $K - \Lambda$, $K - \Lambda'$, and $\Gamma - K$ are accumulated in each curve stacked vertically. Experimental homogeneous linewidths (extrapolated to zero-excitation density) are shown as tangerine (ML) and blue (BL) points.

symmetry leads to energetically degenerate $K'$ and $\Lambda'$ points with opposite spins. We summarize the relevant exciton states in Figs. 3(a) (ML) and 3(c) (BL), and Table 1 in the Supplemental Material [24]. In ML $MoSe_2$, the lowest-energy exciton transition is a direct transition at the $K - K$ point. In contrast, the band structure of BL $MoSe_2$ evolves from a direct to indirect band gap, with the valance band maximum shifting from the $K(K')$ point to the $\Gamma$ point and the conduction band minimum shifting from the $K(K')$ point to the $\Lambda(\Lambda')$ point. The drastic band structure evolution from monolayer to bilayer is attributed to the fact that conduction band at the $\Lambda(\Lambda')$ point and valence band at the $\Gamma$ point are primarily composed of out-of-plane orbitals, while bands at the $K$ point are mainly composed of in plane orbitals [39]. The valley indirect $\Gamma$–$K$, $K$–$\Lambda$, and $\Gamma$–$\Lambda$ excitons are unobservable in the reflectivity and 2D spectra because of their significantly reduced oscillator strength. The key difference between the ML and BL is the emergence of the low-energy valleys in BL. Energetically favorable valley scattering processes become the dominant channel of $A$ exciton decoherence in the BL even at low temperatures and lead to ~6 times faster dephasing than that found in MLs.

We quantitatively evaluate several decoherence channels of the bright $K$–$K$ excitons. By solving Maxwell and Bloch equations, and performing a correlation expansion for the exciton-phonon interaction in the second-order Born-Markov approximation [17], we first calculate the radiative

decay process described in a previous study [47]. Here, we focus on the phonon-assisted decoherence rate in ML and BL [10,47]:

$$\gamma_{\text{phon}}^{K-K} = \sum_{\mathbf{Q},i,\alpha,\pm} |g_{\mathbf{Q}}^{K-K\to i}|^2 \left(\frac{1}{2} \pm \frac{1}{2} + n_{\mathbf{Q}}^{K-i\alpha}\right) \times \mathcal{L}_\gamma(E_{\mathbf{Q}}^{i} - E_{\mathbf{0}}^{K-K} \pm \hbar\Omega_{\mathbf{Q}}^{K-i\alpha}). \quad (2)$$

The summation $i$ incorporates all possible excitonic valleys. In particular it incorporates intravalley scattering ($i = K - K$), intervalley scattering via electron scattering ($i = K - K', K - \Lambda, K - \Lambda'$), and intervalley scattering via hole scattering ($i = K' - K$). The $\pm$ sum accounts for phonon-emission and absorption processes, and $n_{\mathbf{Q}}^{\xi\alpha}$ and $\hbar\Omega_{\mathbf{Q}}^{\xi\alpha}$ account for the phonon occupation and the phonon dispersion at the $\xi$ point in the Brillouin zone and branch $\alpha$ [51]. In the calculation, we include the LA, TA, LO, TO, and A′ modes, which provide the strongest coupling strength in monolayer TMDCs [51]. In this study focusing on quantum decoherence effects in BLs, we assume that the exciton-phonon coupling elements $g_{\mathbf{Q}}^{K-K\to i\alpha}$ appearing in Eq. (2) can be approximated with the according values for the ML material (see the Supplemental Material [24]). The Lorentzian $\mathcal{L}_\gamma(\Delta E)$ with broadening $\gamma$ accounts for the relaxed energy conservation during an exciton-phonon scattering event, while the broadening $\gamma$ is calculated by self-consistently solving Eq. (2) [46].

The results of the calculation are summarized in Fig. 3(b) where each curve plots the accumulative contribution to the linewidth. As an example, the red curve labeled $+K - K$ is a sum of the contribution from radiative decay and the intravalley exciton scattering within the $K$ valleys (see the Supplemental Material [24] for more details). In ML $MoSe_2$, the dephasing rate is mainly determined by the radiative decay and intravalley phonon scattering [52]. At low temperatures, the dephasing rate increases linearly with temperature due to the absorption and emission of long range acoustic phonons [53]. The contribution from intravalley phonon induced decoherence approaches zero as the temperature approaches zero. In contrast, both calculated and measured homogeneous linewidths in BL $MoSe_2$ remain broad ~14 meV even in the low temperature limit, as shown in Fig. 3(d). The self-consistent solution of Eq. (2) reveals that the dominant process is exciton scattering from $K - K$ exciton to $\Gamma - K$ states via emission of acoustic and optical $K$ phonons. Such a phonon-emission process remains efficient even at low temperatures. The coupling to optical phonons here in $MoSe_2$ is stronger than that in $WS_2$, previously studied using linear spectroscopy methods [10]. After investigating exciton-exciton interactions via excitation power dependent measurements (details included in the Supplemental Material [24]), we directly compare the extrapolated and calculated homogeneous linewidth [Figs. 3(b) and 3(d)] in the relevant temperature range, finding remarkable agreement within ~20%. This agreement suggests that the calculations have captured the most important quantum decoherence mechanisms in both the ML and BL.

Next, we extract the exciton population relaxation dynamics by taking zero-quantum spectra. These spectra $S(t_1, \hbar\omega_{t_2}, \hbar\omega_{t_3})$ are acquired by scanning and then applying Fourier transforms with respect to the time delays $t_2$ and $t_3$, while holding $t_1$ constant, as illustrated in Fig. 4(a). Choosing $t_1 = 0$ fs, the zero-quantum spectrum of the $MoSe_2$ BL is presented in Fig. 4(b). As a signature of population relaxation, we observe that the main peak is distributed along the gray dashed line with $\hbar\omega_{t_2} \approx 0$ meV. Examining a line cut through the peak of the exciton resonance along the $\hbar\omega_{t_2}$ direction (blue vertical dashed line), we can further extract the exciton population relaxation rate. Intriguingly, the profile in Fig. 4(c) could only be well fitted with two Lorentzian functions with linewidths of

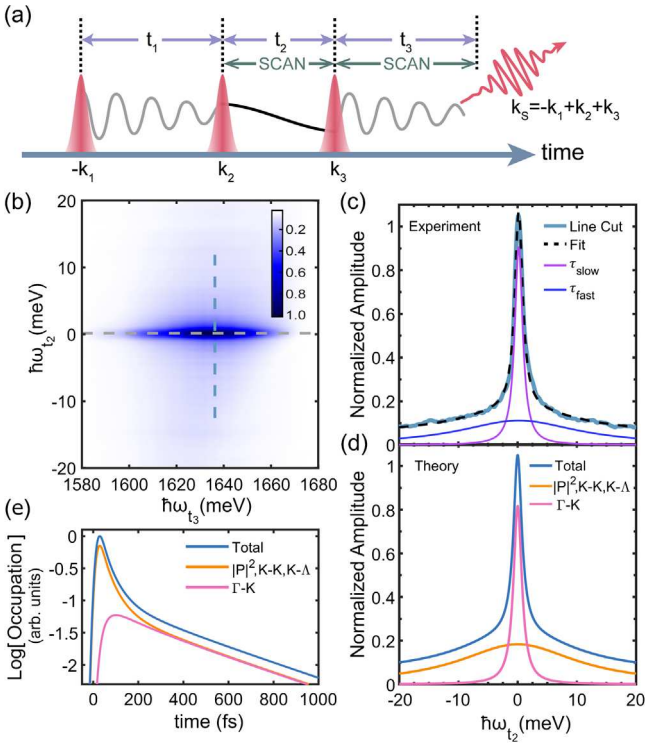


FIG. 4. Zero-quantum spectra from a $MoSe_2$ BL used to extract population relaxation times. (a) Schematic showing the zero-quantum pulse sequence. (b) Zero-quantum spectrum of a $MoSe_2$ BL at $1 \times 10^{12}$ cm$^{-2}$ excitation density and 30 K. The vertical line cut at the peak of the $X^0$ resonance captures population relaxation dynamics. (c) Fitting the zero-quantum line cut with two Lorentzian functions reveals fast $54 \pm 2$ fs and slow $810 \pm 10$ fs decay components. (d) Calculated relaxation dynamics with two dominant components in the frequency domain in excellent agreement with experiment. (e) Theoretical calculation of time-domain population dynamics in the $K$ valley after excitation of $K - K$ excitons. In (c)–(e), the totals are offset from the components for clarity.

12.2 meV and 0.81 meV, respectively. Translating them to decay times, we obtained fast ($\tau_{\text{fast}} = 54 \pm 2$ fs) and slow ($\tau_{\text{slow}} = 810 \pm 10$ fs) components. These timescales are much faster than many previous reports on exciton population relaxation using pump-probe or time-resolved PL techniques [54–56] because our experiments detect third-order coherent signals, enabling a quantitative comparison with microscopic calculations presented below. In contrast, incoherent spectroscopy techniques are often influenced by exciton-repopulation processes from defect-trapped states or conversion from momentum-indirect dark excitons.

Our microscopic calculation begins by determining the Pauli blocking effect in each valley: the blocking is given by the temporal evolution of the overall carrier occupation in the $K$ valley $f = f^e + f^h$, which the third pulse is sensitive to. Electron and hole occupations are determined by the exciton states which have an electron hole in the $K$ valley [57]: $f^e = |P_0^{K-K}|^2 + \sum_{\mathbf{Q},i_h=K,\Gamma} N_{\mathbf{Q}}^{i_h K}$, and $f^h = |P_0^{K-K}|^2 + \sum_{\mathbf{Q},i_e=K,\Lambda,K',\Lambda'} N_{\mathbf{Q}}^{K i_e}$. We find contributions from the optically pumped coherent excitons $P_0^{K-K}$ as well as from incoherent excitons $N_{\mathbf{Q}}^{i_h i_e}$ formed through exciton-phonon scattering of coherent excitons [58]. In our calculation of the temporal evolution of the coherent and incoherent excitons, we include exciton-photon, exciton-phonon, and intervalley exchange interactions [9,58,59]. Our analysis [shown in Fig. 4(d), details in the Supplemental Material [24] ] predicts a fast decay rate of 12.1 meV (55 fs) originating primarily from the decay of coherent excitons, with additional contributions from the relaxation of $K - K$ excitons to momentum-indirect $K - \Lambda$ and $\Gamma - K$ states after the optical pump, and the further decay of $K - \Lambda$ excitons. The subsequent slow decay of 0.85 meV (770 fs) is determined by the decay of the $\Gamma - K$ excitons to the $\Gamma - \Lambda$ exciton states. We present the calculated relaxation processes in the frequency and time domains, as depicted in Figs. 4(d) and 4(e), respectively. There is excellent agreement between the experiments [Fig. 4(c)] and calculation [Fig. 4(d)]. We replotted the calculated dynamics in the time domain for ease of visualization [Fig. 4(e)]. In contrast, exciton population relaxation measured from a $MoSe_2$ ML (details included in the Supplemental Material [24]) reveals a single component decay with a $475 \pm 8$ fs relaxation time, an order of magnitude slower than the 54 fs BL component, emphasizing the distinct microscopic decay channels in the ML and BL.

Early steady-state photoluminescence experiments on TMDC bilayers identified additional exciton resonances attributed to electrons and holes residing in different valleys. [60] Our study goes beyond previous works that suggested interlayer scattering processes should be considered in bilayers. We find that the emergence of additional low-energy valleys in $MoSe_2$ bilayers leads to rapid phonon-assisted intervalley scattering, resulting in significantly faster intrinsic exciton dephasing and two components in the population relaxation dynamics. Microscopic calculations allow us to attribute them to specific intervalley scattering pathways involving $\Lambda$ valley in the conduction band and $\Gamma$ valley in the valence bands. Additional spectroscopy studies such as those based on time-resolved angle-resolved photoemission spectroscopy measurements with momentum space resolution are needed [61–63] to directly visualize these intervalley scattering processes. Understanding how low-energy valleys influence exciton quantum dynamics is critical to extending valleytronics in van der Waals heterostructures beyond the simplest case of "spin-valley locking" found in TMDC MLs.

The spectroscopic experiments performed by K. S. at UT-Austin were supported by NSF DMR-1808042, and D. H. is supported by the Department of Energy, Basic Energy Science program via grant DE-SC0019398. K. S. acknowledges the support of a fellowship via NSF DMR-1747426. The facility for preparing the sample was primarily supported by the NSF MRSEC program DMR-1720595, and consumable materials were purchased using funding provided by the Welch Foundation via F-1662. Funding for S. H., U. W., and N. O. was provided by Deutsche Forschungsgemeinschaft via the GRK 1558, the CRC 787. We acknowledge funding from the Deutsche Forschungsgemeinschaft via Project No. 182087777 in SFB 951 (Project No. B12, M. S., and A. K.). E. M. acknowledges the support from European Unions Horizon 2020 research and innovation program under Grant Agreement No. 881603 (Graphene Flagship) and Deutsche Forschungsgemeinschaft via CRC 1083. M. S. acknowledges fruitful discussions within the priority program SPP 2244 of the Deutsche Forschungsgemeinschaft.

S. H. and K. S. contributed equally to this work.

*nina.owschimikow@physik.tu-berlin.de
†elaineli@physics.utexas.edu

[1] G. Wang, A. Chernikov, M. M. Glazov, T. F. Heinz, X. Marie, T. Amand, and B. Urbaszek, Rev. Mod. Phys. **90**, 021001 (2018).
[2] T. Mueller and E. Malic, npj 2D Mater. Appl. **2**, 29 (2018).
[3] H. Zeng, J. Dai, W. Yao, D. Xiao, and X. Cui, Nat. Nanotechnol. **7**, 490 (2012).
[4] K. F. Mak, K. He, J. Shan, and T. F. Heinz, Nat. Nanotechnol. **7**, 494 (2012).
[5] D. Xiao, G.-B. Liu, W. Feng, X. Xu, and W. Yao, Phys. Rev. Lett. **108**, 196802 (2012).
[6] T. Cao, G. Wang, W. Han, H. Ye, C. Zhu, J. Shi, Q. Niu, P. Tan, E. Wang, B. Liu, and J. Feng, Nat. Commun. **3**, 887 (2012).
[7] K. F. Mak, C. Lee, J. Hone, J. Shan, and T. F. Heinz, Phys. Rev. Lett. **105**, 136805 (2010).
[8] A. Splendiani, L. Sun, Y. Zhang, T. Li, J. Kim, C.-Y. Chim, G. Galli, and F. Wang, Nano Lett. **10**, 1271 (2010).

[9] M. Selig, F. Katsch, R. Schmidt, S. M. de Vasconcellos, R. Bratschitsch, E. Malic, and A. Knorr, Phys. Rev. Research **1**, 022007(R) (2019).

[10] A. Raja, M. Selig, G. Berghäuser, J. Yu, H. M. Hill, A. F. Rigosi, L. E. Brus, A. Knorr, T. F. Heinz, E. Malic, and A. Chernikov, Nano Lett. **18**, 6135 (2018).

[11] C. M. Chow, H. Yu, A. M. Jones, J. R. Schaibley, M. Koehler, D. G. Mandrus, R. Merlin, W. Yao, and X. Xu, npj 2D Mater. Appl. **1**, 33 (2017).

[12] S. Brem, A. Ekman, D. Christiansen, F. Katsch, M. Selig, C. Robert, X. Marie, B. Urbaszek, A. Knorr, and E. Malic, Nano Lett. **20**, 2849 (2020).

[13] G. Moody, C. K. Dass, K. Hao, C.-H. Chen, L.-J. Li, A. Singh, K. Tran, G. Clark, X. Xu, G. Berghäuser, E. Malic, A. Knorr, and X. Li, Nat. Commun. **6**, 8315 (2015).

[14] K. Hao, G. Moody, F. Wu, C. K. Dass, L. Xu, C.-H. Chen, L. Sun, M.-Y. Li, L.-J. Li, A. H. Macdonald, and X. Li, Nat. Phys. **12**, 677 (2016).

[15] K. Hao, L. Xu, P. Nagler, A. Singh, K. Tran, C. K. Dass, C. Schller, T. Korn, X. Li, and G. Moody, Nano Lett. **16**, 5109 (2016).

[16] M. Titze, B. Li, X. Zhang, P. M. Ajayan, and H. Li, Phys. Rev. Mater. **2**, 054001 (2018).

[17] M. Selig, G. Berghuser, M. Richter, R. Bratschitsch, A. Knorr, and E. Malic, 2D Mater. **5**, 035017 (2018).

[18] S. Brem, M. Selig, G. Berghaeuser, and E. Malic, Sci. Rep. **8**, 8238 (2018).

[19] F. Katsch, M. Selig, and A. Knorr, Phys. Rev. Lett. **124**, 257402 (2020).

[20] J. Lindlau, M. Selig, A. Neumann, L. Colombier, J. Förste, V. Funk, M. Förg, J. Kim, G. Berghäuser, T. Taniguchi, K. Watanabe, F. Wang, E. Malic, and A. Hgele, Nat. Commun. **9**, 2586 (2018).

[21] R. Roldn, J. A. Silva-Guilln, M. P. Lpez-Sancho, F. Guinea, E. Cappelluti, and P. Ordejn, Ann. Phys. (Berlin) **526**, 347 (2014).

[22] J. Sung, Y. Zhou, G. Scuri, V. Zlyomi, T. I. Andersen, H. Yoo, D. S. Wild, A. Y. Joe, R. J. Gelly, H. Heo, S. J. Magorrian, D. Brub, A. M. M. Valdivia, T. Taniguchi, K. Watanabe, M. D. Lukin, P. Kim, V. I. Falko, and H. Park, Nat. Nanotechnol. **15**, 750 (2020).

[23] T. I. Andersen, G. Scuri, A. Sushko, K. De Greve, J. Sung, Y. Zhou, D. S. Wild, R. J. Gelly, H. Heo, D. Brub, A. Y. Joe, L. A. Jauregui, K. Watanabe, T. Taniguchi, P. Kim, H. Park, and M. D. Lukin, Nat. Mater. **20**, 480 (2021).

[24] See Supplemental Material at http://link.aps.org/supplemental/10.1103/PhysRevLett.127.157403 for sample images, theoretical treatment of the dephasing and relaxation mechanisms, and additional measurements, which includes Refs. [25–36].

[25] N. S. Rytova, Moscow Univ. Phys. Bull. **3**, 18 (1967).

[26] S. Rudin, T. L. Reinecke, and B.Segall, Phys. Rev. B **42**, 11218 (1990).

[27] M. L. Trolle, T. G. Pedersen, and V. Veniard, Sci. Rep. **7**, 39844 (2017).

[28] Y. Li, A. Chernikov, X. Zhang, A. Rigosi, H. M. Hill, A. M. van der Zande, D. A. Chenet, E.-M. Shih, J. Hone, and T. F. Heinz, Phys. Rev. B **90**, 205422 (2014).

[29] J. Lee, E. S. Koteles, and M. O. Vassell, Phys. Rev. B **33**, 5512 (1986).

[30] A. Kormanyos, G. Burkard, M. Gmitra, J. Fabian, V. Zolyomi, N. D. Drummond, and V. Falko, 2D Mater. **2**, 022001 (2015).

[31] Z. Jin, X. Li, J. T. Mullen, and K. W. Kim, Phys. Rev. B **90**, 045422 (2014).

[32] V. Srinivas, J. Hryniewicz, Y. J. Chen, and C. E. C. Wood, Phys. Rev. B **46**, 10193 (1992).

[33] Z. Khatibi, M. Feierabend, M. Selig, S. Brem, C. Linderlv, P. Erhart, and E. Malic, 2D Mater. **6**, 015015 (2018).

[34] S. Helmrich, R. Schneider, A. W. Achtstein, A. Arora, B. Herzog, S. M. de Vasconcellos, M. Kolarczik, O. Schps, R. Bratschitsch, U. Woggon, and N. Owschimikow, 2D Mater. **5**, 045007 (2018).

[35] D. Erkensten, S. Brem, and E. Malic, Phys. Rev. B **103**, 045426 (2021).

[36] T. Stroucken, A. Knorr, P. Thomas, and S. W. Koch, Phys. Rev. B **53**, 2026 (1996).

[37] A. Arora, K. Nogajewski, M. Molas, M. Koperski, and M. Potemski, Nanoscale **7**, 20769 (2015).

[38] Y. Niu, S. Gonzalez-Abad, R. Frisenda, P. Marauhn, M. Drüppel, P. Gant, R. Schmidt, N. S. Taghavi, D. Barcons, A. J. Molina-Mendoza *et al.*, Nanomater. Nanotechnol. **8**, 725 (2018).

[39] S. K. Pandey, R. Das, and P. Mahadevan, ACS Omega **5**, 15169 (2020).

[40] J. P. Perdew, W. Yang, K. Burke, Z. Yang, E. K. Gross, M. Scheffler, G. E. Scuseria, T. M. Henderson, I. Y. Zhang, A. Ruzsinszky *et al.*, Proc. Natl. Acad. Sci. U.S.A. **114**, 2801 (2017).

[41] K. Hao, J. F. Specht, P. Nagler, L. Xu, K. Tran, A. Singh, C. K. Dass, C. Schller, T. Korn, M. Richter, A. Knorr, X. Li, and G. Moody, Nat. Commun. **8**, 15552 (2017).

[42] T. Jakubczyk, G. Nayak, L. Scarpelli, W.-L. Liu, S. Dubey, N. Bendiab, L. Marty, T. Taniguchi, K. Watanabe, F. Masia, G. Nogues, J. Coraux, W. Langbein, J. Renard, V. Bouchiat, and J. Kasprzak, ACS Nano **13**, 3500 (2019).

[43] M. E. Siemens, G. Moody, H. Li, A. D. Bristow, and S. T. Cundiff, Opt. Express **18**, 17699 (2010).

[44] J. S. Ross, S. Wu, H. Yu, N. J. Ghimire, A. M. Jones, G. Aivazian, J. Yan, D. G. Mandrus, D. Xiao, W. Yao, and X. Xu, Nat. Commun. **4**, 1474 (2013).

[45] M. Cho, Chem. Rev. **108**, 1331 (2008).

[46] E. W. Martin, J. Horng, H. G. Ruth, E. Paik, M.-H. Wentzel, H. Deng, and S. T. Cundiff, Phys. Rev. Applied **14**, 021002 (R) (2020).

[47] M. Selig, G. Berghäuser, A. Raja, P. Nagler, C. Schüller, T. F. Heinz, T. Korn, A. Chernikov, E. Malic, and A. Knorr, Nat. Commun. **7**, 13279 (2016).

[48] Y. Zhang, T.-R. Chang, B. Zhou, Y.-T. Cui, H. Yan, Z. Liu, F. Schmitt, J. Lee, R. Moore, Y. Chen, H. Lin, H.-T. Jeng, S.-K. Mo, Z. Hussain, A. Bansil, and Z.-X. Shen, Nat. Nanotechnol. **9**, 111 (2014).

[49] J. He, K. Hummer, and C. Franchini, Phys. Rev. B **89**, 075409 (2014).

[50] S. Ovesen, S. Brem, C. Linderlv, M. Kuisma, T. Korn, P. Erhart, M. Selig, and E. Malic, Commun. Phys. **2**, 23 (2019).

[51] Z. Jin, X. Li, J. T. Mullen, and K. W. Kim, Phys. Rev. B **90**, 045422 (2014).

[52] T. Jakubczyk, V. Delmonte, M. Koperski, K. Nogajewski, C. Faugeras, W. Langbein, M. Potemski, and J. Kasprzak, Nano Lett. **16**, 5333 (2016).
[53] P. Dey, J. Paul, Z. Wang, C. E. Stevens, C. Liu, A. H. Romero, J. Shan, D. J. Hilton, and D. Karaiskaj, Phys. Rev. Lett. **116**, 127402 (2016).
[54] H. Shi, R. Yan, S. Bertolazzi, J. Brivio, B. Gao, A. Kis, D. Jena, H. G. Xing, and L. Huang, ACS Nano **7**, 1072 (2013).
[55] C. Robert, D. Lagarde, F. Cadiz, G. Wang, B. Lassagne, T. Amand, A. Balocchi, P. Renucci, S. Tongay, B. Urbaszek, and X. Marie, Phys. Rev. B **93**, 205423 (2016).
[56] G. Wang, E. Palleau, T. Amand, S. Tongay, X. Marie, and B. Urbaszek, Appl. Phys. Lett. **106**, 112101 (2015).
[57] F. Katsch, M. Selig, A. Carmele, and A. Knorr, Phys. Status Solidi (b) **255**, 1800185 (2018).
[58] M. Selig, G. Berghäuser, M. Richter, R. Bratschitsch, A. Knorr, and E. Malic, 2D Mater. **5**, 035017 (2018).
[59] M. Selig, F. Katsch, S. Brem, G. F. Mkrtchian, E. Malic, and A. Knorr, Phys. Rev. Research **2**, 023322 (2020).
[60] D. Kozawa, R. Kumar, A. Carvalho, K. K. Amara, W. Zhao, S. Wang, M. Toh, R. M. Ribeiro, A. C. Neto, K. Matsuda *et al.*, Nat. Commun. **5**, 4543 (2014).
[61] J. Madéo, M. K. Man, C. Sahoo, M. Campbell, V. Pareek, E. L. Wong, A. A. Mahboob, N. S. Chan, A. Karmakar, B. M. K. Mariserla, X. Li, T. F. Heinz, T. Cao, and K. M. Dani, Science **370**, 1199 (2020).
[62] S. Dong, M. Puppin, T. Pincelli, S. Beaulieu, D. Christiansen, H. Hubener, C. W. Nicholson, R. P. Xian, M. Dendzik, Y. Deng, Y. W. Windsor, M. Selig, E. Malic, A. Rubio, A. Knorr, M. Wolf, L. Rettig, and R. Ernstorfer, Natural sciences **1**, e10010 (2021).
[63] R. Wallauer, R. Perea-Causin, L. Mnster, S. Zajusch, S. Brem, J. Gdde, K. Tanimura, K. Lin, R. Huber, E. Malic, and U. Hfer, Nano Lett. **21**, 5867 (2021).